The Astronomical Journal, 146:12 (16pp), 2013 July doi:10.1088/0004-6256/146/1/12

KRONOSEISMOLOGY: USING DENSITY WAVES IN SATURN'S C RING TO PROBE THE PLANET'S INTERIOR

M. M. Hedman and P. D. Nicholson
Center for Radiophysics and Space Research, Cornell University, Ithaca, NY 14850, USA; mmhedman@astro.cornell.edu
Received 2013 March 15; accepted 2013 April 12; published 2013 June 11

ABSTRACT

Saturn's C ring contains multiple spiral patterns that appear to be density waves driven by periodic gravitational perturbations. In other parts of Saturn's rings, such waves are generated by Lindblad resonances with Saturn's various moons, but most of the wave-like C-ring features are not situated near any strong resonance with any known moon. Using stellar occultation data obtained by the Visual and Infrared Mapping Spectrometer on board the *Cassini* spacecraft, we investigate the origin of six unidentified C-ring waves located between 80,900 and 87,200 km from Saturn's center. By measuring differences in the waves' phases among the different occultations, we are able to determine both the number of arms in each spiral pattern and the speeds at which these patterns rotate around the planet. We find that all six of these waves have between two and four arms and pattern speeds between 1660° day^{-1} and 1861° day^{-1}. These speeds are too large to be attributed to any satellite resonance. Instead, they are comparable to the predicted pattern speeds of waves generated by low-order normal-mode oscillations within the planet. The precise pattern speeds associated with these waves should therefore provide strong constraints on Saturn's internal structure. Furthermore, we identify multiple waves with the same number of arms and very similar pattern speeds, indicating that multiple $m = 3$ and $m = 2$ sectoral ($l = m$) modes may exist within the planet.

Key words: planets and satellites: interiors – planets and satellites: rings

Online-only material: color figures, machine-readable and VO tables, Supplemental data file

1. INTRODUCTION

Spiral waves are patterns in Saturn's rings produced by periodic gravitational perturbations on the ring material. Many of these waves can be attributed to mean-motion resonances with Saturn's various moons. However, a number of spiral waves in the C ring do not fall near any known resonance with any moon. These waves were first noticed in the *Voyager* radio occultation data (Rosen et al. 1991), but have also been observed in stellar occultations by the ultraviolet spectrometer on board the *Cassini* spacecraft (Colwell et al. 2009b; Baillié et al. 2011). However, these previous studies were unable to identify the source of the perturbations responsible for generating these waves because they could not determine either the number of arms in the spirals or how fast the relevant patterns were rotating around the planet. Using occultation data from the Visual and Infrared Mapping Spectrometer (VIMS), we have now been able to determine both these quantities for six of these unidentified waves. These six waves have the right pattern speeds and symmetry properties to be produced by low-order normal mode oscillations within Saturn, as predicted by Marley (1990) and Marley & Porco (1993). These waves should therefore provide valuable new constraints on the planet's interior structure.

Prior to describing our analysis of these waves, we first provide some background information about the relevant spiral waves in Section 2. This includes a brief summary of the theory behind spiral waves (Section 2.1), a summary of the wave-like features in the C ring (Section 2.2) and a description of the six waves that will be investigated here (Section 2.3). Section 3 then describes how we can determine the number of arms and pattern speeds of these waves. Section 3.1 describes the VIMS occultation data that will be used in this analysis. Section 3.2 illustrates how comparing multiple occultations can constrain the waves' symmetry properties using a particularly informative set of occultations. Sections 3.3 and 3.4 describe the wavelet-based techniques we employ to ascertain the number of arms and pattern speeds of these waves. Section 4 summarizes the results of our calculations. Finally, Section 5 discusses the implications of our findings.

2. BACKGROUND

2.1. The Theory of Spiral Waves

Spiral patterns in Saturn's rings are generated by various periodic perturbations on the ring material, and different types of perturbations produce different types of spiral waves. For example, periodic vertical forces generate warped structures known as bending waves, while periodic radial or azimuthal forces produce variations in the rings' surface density known as density waves. The structure and dynamics of these spiral patterns are relatively well understood and good theoretical overviews of these phenomena are available (e.g., Shu 1984). Hence, we will only briefly review the aspects of spiral waves that are most relevant to this analysis. Note that the waves considered below all appear to be density waves, so we will focus on the dynamics of those structures here.

A given spiral density wave consists of an integer number of arms that become more tightly wrapped with increasing distance from the radius of the exact resonance. This entire pattern rotates around the planet at a single pattern speed. The waves in Saturn's rings are so tightly wrapped that the opacity variations appear to be almost purely radial in both images and occultation profiles. Hence, the waves appear as periodic variations in ring brightness or opacity whose wavelength changes systematically with radius (see Figure 1 below for some examples). However, because a density wave is actually a rotating spiral pattern, the locations of the peaks and troughs in a given profile will depend on both the observed ring longitude and the orientation of the pattern during the measurement.

The organized motions responsible for spiral density waves are most efficiently generated by Lindblad resonances. At these resonances, the ring-particles' radial epicyclic frequency κ is an

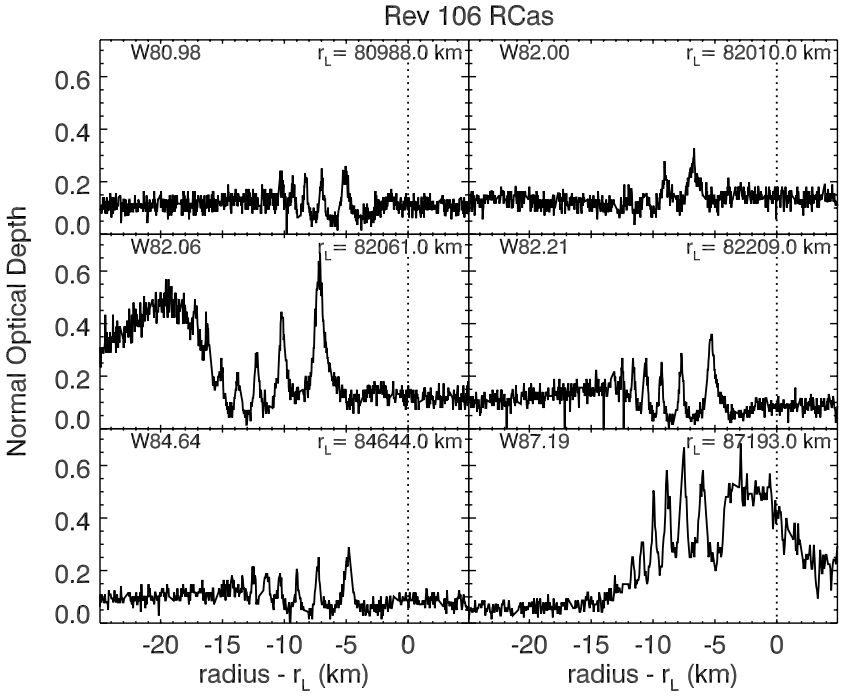

Figure 1. VIMS occultation profiles of the six waves examined in this analysis. Each panel shows the ring's normal optical depth vs. ring radius, which is measured in kilometers from the inferred resonance location r_L. (For the innermost five waves, the r_L value comes from Baillié et al. 2011, while for W87.19 the resonance position has been adjusted to match the best-fit pattern speed of this wave, see Section 4.) The specific profiles shown here come from an occultation by the rings of the star R Cassiopaea, which provides our highest-resolution profiles of these waves. The raw data numbers were converted to transmission estimates by normalizing the stellar signal to unity in the middle of the Maxwell Gap (87,375–87,425 km), and then translated to normal optical depth values using the standard formula, assuming the elevation angle of the star is 56.°04 above the ringplane.

(Supplemental data of this figure are available in the online journal.)

integer multiple of the difference between the angular frequency of the perturbing potential Ω_p and the ring-particles' mean motion n. Hence, if there is a density wave driven at a given radial location in the rings, then the most likely resonant perturbation frequencies will satisfy the following relationship:

$$m(n - \Omega_p) = \kappa, \tag{1}$$

where m is any non-zero integer (i.e., $m = \ldots, -3, -2, -1, 1, 2, 3, \ldots$). Rewriting the resonant condition in terms of the local apsidal precession rate, $\dot{\varpi} = n - \kappa$, we have the familiar expression for a first-order Lindblad resonance:

$$(m - 1)n + \dot{\varpi} = m\Omega_p. \tag{2}$$

Since $\dot{\varpi} \ll n$, resonances with $m > 0$ (known as inner Lindblad resonances or ILRs) have $\Omega_p \approx (m - 1)n/m$, while those with $m < 0$ (known as outer Lindblad resonances or OLRs) have $\Omega_p \approx (|m| + 1)n/|m|$.

In a differentially rotating, self-gravitating disk, the periodic perturbations at such a resonance give rise to a trailing spiral density wave that propagates away from the location of the exact resonance toward the location in the rings where $n = \Omega_p$. Thus, for a Keplerian disk like Saturn's rings (and assuming $\Omega_p > 0$), density waves will propagate outward from an inner Lindblad resonance and inward from an outer Lindblad resonance. The pattern of surface density variations generated by such a wave gives rise to variations in the local optical depth with radius r, inertial longitude λ, and time t. For waves of small amplitude these variations may be written as

$$\tau(r, \lambda, t) \simeq \tau_0 + \Delta\tau(r) \cos \phi(r, \lambda, t), \tag{3}$$

where the wave's phase ϕ can be decomposed into a part that depends only on the observed longitude and time, and another that depends only on radius:

$$\phi(r, \lambda, t) \simeq |m|(\lambda - \Omega_p t) + \phi_r(r). \tag{4}$$

Hence, $|m|$ gives the number of arms in the wave pattern, while Ω_p is the angular rate at which it rotates around the planet. The wave's pattern speed therefore equals the angular frequency of the external perturbing force.

At sufficiently large distances from the resonance, the radius-dependent part of the phase is given by the following asymptotic expression:

$$\phi_r(r) \simeq \left[3(m - 1) + J_2 \frac{21}{2} \left(\frac{r_S}{r_L}\right)^2\right] \frac{M_S (r - r_L)^2}{4\pi\sigma_0 r_L^4} + \phi_0, \tag{5}$$

where M_S is the mass of Saturn, J_2 is a measure of the planet's oblateness, $r_S = 60{,}330$ km, r_L is the resonant radius where Equation (1) is satisfied, σ_0 is the undisturbed surface mass density of the ring, and ϕ_0 is a constant. Note that for an outward-propagating wave from an ILR, both $m - 1$ and $r - r_L$ are positive, while for an inward-propagating wave from an OLR $m - 1$ and $r - r_L$ are both negative. Hence, in both cases, $d\phi/dr > 0$ and a line of constant phase will have $dr/d\lambda < 0$, corresponding to a trailing wave pattern. Also, the wave's radial wavenumber k derived from the above expression:

$$k(r) = \frac{d\phi}{dr} \simeq \left[3(m - 1) + J_2 \frac{21}{2} \left(\frac{r_S}{r_L}\right)^2\right] \frac{M_S (r - r_L)}{2\pi\sigma_0 r_L^4}, \tag{6}$$

increases linearly with distance from r_L.

Table 1
Summary of Waves Investigated Here, Including Designations by Various Authors

Wave Location[a]	Rosen et al. (1991)[b]	Colwell et al. (2009b)	Baillié et al. (2011)
80988 km	e	W80.98	13
82010 km		W82.00	15
82061 km	f	W82.06	16
82209 km	g	W82.21	17
84644 km	i	W84.64	19
87189 km		W87.19	32

Notes.
[a] Inferred resonance location obtained by fitting Equation (6) to UVIS occultation data, see Table 7 of Baillié et al. (2011).
[b] See Figures 7 and 8 in Rosen et al. (1991).

So long as the background opacity of the ring τ_o does not vary too much with radius, the phase parameter ϕ can be computed directly from the local opacity variations (e.g., opacity maxima occur where $\phi \simeq 0$ and opacity minima occur where $\phi \simeq 180^\circ$). Thus $\phi(r, \lambda)$ can be calculated from any given radial profile across the ring. Indeed, for identifiable waves the trends in ϕ with radius can be used to estimate parameters like the ring's surface mass density (Tiscareno et al. 2007). However, for our efforts to determine the pattern speeds and m-values of unidentified waves, it is more useful to consider the difference in phase parameters between occultations observed at different times and longitudes. For these phase differences $\delta\phi$, the radius-dependent term ϕ_r should cancel out, leaving terms that only depend on the known differences in the observation times (δt) and observed longitudes ($\delta\lambda$), and the unknown parameters $|m|$ and Ω_p:

$$\delta\phi = |m|(\delta\lambda - \Omega_p \delta t). \quad (7)$$

We can therefore compare the observed phase differences $\delta\phi$ with those predicted for various combinations of m and Ω_p, and thereby determine which pattern speed and m-number is most consistent with the observed phase differences.

2.2. Spiral Waves in the C Ring

Surveys of Saturn's C ring by Rosen et al. (1991), Colwell et al. (2009b) and Baillié et al. (2011) have found a total of 27 wave-like structures in the C ring. Only five of these features have been identified with specific satellite resonances. The most prominent feature is a bending wave generated by an unusual Titan −1:0 nodal resonance (Rosen & Lissauer 1988), and Rosen et al. (1991) identified one density wave produced by the Mimas 4:1 ILR. More recently, the density wave produced by the Atlas 2:1 ILR has been detected, and there are hints of density waves at the locations of the Mimas 6:2 and Pandora 4:1 resonances (Colwell et al. 2009b; Baillié et al. 2011). More than half of the remaining unidentified waves appear to be inward-propagating (i.e., their radial wavenumber increases inward). Such behavior is inconsistent with density waves generated by resonances with Saturn's moons. Since all the moons orbit outside the rings, the perturbation frequency associated with any moon's gravitational perturbations will be smaller than the local orbital frequency anywhere in the C ring. Hence, Lindblad resonances in the C ring with any moon should be ILRs, which should generate outward-propagating waves. The inward-propagating waves must therefore be produced by some other mechanism.

One possible explanation for these inward-propagating waves is that they are bending waves instead of density waves. Unlike density waves, bending waves typically propagate away from the location in the rings where $\Omega_p = n$ (Shu 1984). Hence, vertical resonances where the perturbation frequency is less than the local orbital frequency (the so-called inner Vertical resonances or IVRs), like those generated by several of Saturn's moons, should propagate inward. Furthermore, the very low ring opening angle in the *Voyager* radio experiment ($B = 5.^\circ 6$) meant that the vertical warps in the bending wave could lead to significant optical depth variations along the observed line of sight. However, most of these inward-propagating waves are also clearly visible in stellar occultations observed by *Cassini* at high ring opening angles, where optical depth variations from bending waves would be very subtle.[1] Furthermore, there are no strong candidate IVRs due to known (or even hypothesized) satellites at the desired locations. Thus, this is not the currently favored interpretation for most of these inward-propagating features.

An alternative explanation of these waves is that they are not generated by resonances with Saturn's moons, but instead are produced by resonances with normal-mode oscillations within Saturn itself. Stevenson (1982) first suggested that oscillations within the planet could produce identifiable structures in the rings. Later, Marley (1990, 1991) and Marley & Porco (1993) demonstrated that acoustic modes in the planet's interior could indeed give rise to gravitational perturbations with pattern speeds that are sufficiently fast to generate OLRs and inward-propagating waves in the C ring. The latter authors also found that the predicted pattern speeds of low-degree f-modes were consistent with some of the observed wave locations, but uncertainties in Saturn's interior structure and in the theory of normal modes meant that the resonance radii could only be predicted to within ∼500 km.

2.3. The Six Waves Examined in this Study

This analysis will focus on six of the unidentified, inward-propagating waves. As summarized in Table 1, these waves have been designated in various ways by different authors. Here we will use the Colwell et al. (2009b) nomenclature, which identifies each wave with a number giving the radial location of the wave in thousands of kilometers. Figure 1 shows profiles of all six waves derived from the highest resolution VIMS occultation to date (see below for how these data were processed). Each wave appears as a periodic variation in the ring's opacity, with a wavelength that varies with distance from the planet. More specifically, all these waves have wavelengths that decrease inward, which suggests that they are either bending waves driven by IVRs or density waves driven by OLRs. Since the visibility of these waves does not appear to vary with spacecraft elevation angle, it is unlikely that any of these features are bending waves. Indeed, their pattern speeds turn out to be consistent with those expected for OLRs. Hence, for the remainder of this discussion we will anticipate our final result by referring to these features as density waves.

All six waves are located in the central part of the C ring, between radii of 80,900 and 87,200 km. This is a region of gently undulating structure, with an average normal optical depth (i.e., the optical depth the ring would have if the line of sight was

[1] One exception is the wave designated "j" in Rosen et al. (1991), which is in fact invisible in all VIMS occultation profiles obtained to date, but is seen in one or more UVIS stellar occultations observed at very low opening angles (Baillié et al. 2011).

exactly perpendicular to the ringplane) of about 0.10. All but the outermost wave are located between the "plateau" features designated P4 and P5 by Colwell et al. (2009b). While four of the waves fall in otherwise unexceptional locations, two fall either on top of (W87.19) or immediately adjacent to (W82.06) local maxima in optical depth.

The strongest known eccentric resonances in this region are the two fourth-order Enceladus 5:1 resonances at 82,538 and 82,477 km, the third-order Janus and Epimetheus 5:2 resonances at ~82,780 km and ~82,950 km, the Pan 2:1 ILR at 85,105 km, and the Atlas 2:1 ILR at 87,647 km. Only the last of these is known to be associated with an observable wave. None of these resonances is located within 100 km of any of the unidentified waves. There are two very weak vertical resonances in the vicinity of our target waves: the Enceladus 5:1(e^2i) resonance at 80,967 km (located 21 km interior to the W80.98 wave), and the Janus 5:2(ei) resonance at 82,096–82,107 km (~40 km exterior to the W82.06 wave). However, as mentioned above, the visibility of these waves at large ring opening angles argues against these features being bending waves, and furthermore many other comparable (or stronger) vertical resonances do not produce visible bending waves in the rings. Hence, we consider these rough alignments to be coincidental, and conclude that none of these six waves can be attributed to a resonance with any of Saturn's moons.

These six waves have the strongest opacity variations and the longest wavelengths of any of the unidentified C-ring waves. We focus exclusively on these waves because they provide the best opportunities for determining unambiguous pattern speeds. The strong opacity variations mean that we can clearly detect the maxima and minima, which makes the relevant phase parameters easier to determine. Furthermore, the relatively long wavelengths of these waves should minimize our sensitivity to small errors in the occultation geometry. Errors in *Cassini*'s trajectory reconstruction can cause the occultation profiles to shift slightly in radius, which can in turn create problems when comparing data from different occultations. For example, if one profile was shifted relative to the other by half a wavelength, then the phase difference between the waves might appear to be zero when in reality it is 180°. However, this is unlikely to occur with any of these six waves, because they all have maximum wavelengths exceeding 2 km, which is considerably larger than the subkilometer uncertainties in our reconstructions of occultation geometry (see below).

3. METHODS

3.1. VIMS Observations

The VIMS instrument is described in detail in Brown et al. (2004). While VIMS is typically used to obtain spatially resolved spectra of a scene, it can also operate in an "occultation mode" where the short-wavelength VIS channel is turned off, while the longer-wavelength IR channel stares at a single pixel targeted at a star and obtains a series of rapidly sampled near-infrared stellar spectra at 31 wavelengths between 0.85 and 5.0 μm. As the star moves behind the rings, its apparent brightness varies due to variations in the ring's opacity. Note that the response of the detector is highly linear, so after a constant instrumental background is removed from each spectral channel, the data numbers returned by the instrument are proportional to the incident flux. In order to avoid contamination from sunlight scattered by the rings, we focus exclusively on data from one spectral channel covering the range 2.87–3.00 μm, where water ice is strongly absorbing. The rings are sufficiently dark at these wavelengths so that ringshine is negligible, and the measured signal is directly proportional to the transmission through the rings T. We can therefore easily translate the raw data numbers into the slant optical depth along the line of sight through the rings $\tau = -\ln(T)$, or the normal optical depth of the rings $\tau_n = \tau \sin B$ (B = elevation angle of the star above the rings).

A precise time stamp is appended to each spectrum, facilitating the geometry reconstruction. Using the appropriate SPICE kernels, we can compute the radius where the starlight pierced the ringplane for each sample in the given occultation. This calculation accounts for the light travel time from the rings to *Cassini*, and uses stellar positions taken from the Hipparcos catalog[2], corrected for parallax at Saturn. The positions of sharp edges of gaps and ringlets in the Cassini Division and C ring demonstrate that the resulting reconstructed geometry for each occultation is accurate to within a kilometer (Nicholson et al. 2011; French et al. 2011). R. G. French et al. (in preparation) have used a sub-set of these sharp features to make small corrections to the spacecraft's position during these occultations. These corrections not only reduce the dispersion in the radial position estimates of sharp edges to ~150 m, but also yield more consistent estimates of the density wave phases (see below).

Between 2005 and 2009, VIMS obtained a total of 27 occultation cuts through the C ring with sufficient signal-to-noise and spatial resolution to discern the relevant waves. Table 2 provides a list of these occultations, identifying the star observed, the "Rev number" (*Cassini*'s orbit around Saturn) when the data were obtained, and whether the cut was obtained during ingress or egress. The table also provides the ephemeris time and observed inertial longitude when the star passed behind each of the six waves discussed below. Blank entries in this table correspond to cases where the occultation did not cover the particular wave or when a data gap corrupted the relevant profile, and thus were excluded from this analysis.

3.2. Initial Examination of the Waves Using RS Cancri Occultations

Before describing the procedures we will use to determine the m-numbers and pattern speeds of the waves from these occultation data, let us first examine some particularly informative occultations of the star RS Cancri. Unlike the other occultations considered in this analysis, these were chord occultations where the star cut obliquely through the rings. In such an occultation, the star passes through the same radial range at two very different longitudes as the track enters and then leaves the rings. Comparisons of the wave profiles derived from the ingress and egress parts of these occultations thus provide illustrative examples of how occultation data can constrain wave parameters. Furthermore, even simple visual inspections of these wave profiles indicates that several of the unidentified waves have very similar pattern speeds and likely the same m-numbers.

Figures 2 and 3 show the relevant occultation profiles from the RS Cancri occultations observed during Revs 80 and 85 (the Rev 87 RS Cancri occultation only probed waves exterior to 84,000 km and is not shown here). Of particular interest are the three waves W82.00, W82.06 and W82.20, which are clustered within a region a couple of hundred kilometers wide around 82,100 km. In the Rev 80 RS Cancri data, the ingress and egress profiles for each of these waves are almost perfectly anti-correlated, with peaks in one profile corresponding to dips in

[2] http://heasarc.gsfc.nasa.gov/W3Browse/all/hipparcos.html

Table 2
Observed Times (in Seconds of Ephemeris Time, Measured from the J2000 Epoch) and Inertial Longitudes (Measured Relative to the Longitude of Ascending Node on J2000) for the Various Occultation Cuts Through each Wave

Star	Rev	i/e	W80.98	W82.00	W82.06	W82.21	W84.64	W87.19
R Hya	036	i	220948260. 174.°072	220948093. 175.°060	220948085. 175.°108	220948061. 175.°249	220947679. 177.°407	220947295. 179.°453
α Aur	041	i	227949007. 343.°813	227948789. 345.°077	227948779. 345.°137	227948748. 345.°316	227948261. 348.°013	227947783. 350.°513
γ Cru	071	i	266193414. 183.°104	266193267. 183.°241	266193260. 183.°248	266193238. 183.°267	266192889. 183.°578	266192521. 183.°886
γ Cru	073	i	267426088. 182.°136	267425942. 182.°281	267425935. 182.°288	267425913. 182.°309	267425565. 182.°640	267425200. 182.°969
γ Cru	077	i	269858216. 181.°086	269858071. 181.°240	269858064. 181.°247	269858043. 181.°269	269857699. 181.°619	269857336. 181.°965
γ Cru	078	i	270466692. 180.°860	270466548. 181.°015	270466541. 181.°023	270466520. 181.°045	270466176. 181.°398	270465814. 181.°747
β Gru	078	i					270512795. 302.°800	270512284. 294.°401
γ Cru	079	i	271045522. 179.°175	271045367. 179.°354	271045359. 179.°363	271045337. 179.°389	271044968. 179.°795	271044581. 180.°198
RS Cnc	080	i	271872473. 90.°240	271872088. 87.°858	271872070. 87.°749	271872018. 87.°431	271871265. 82.°984	
RS Cnc	080	e	271877226. 121.°515	271877611. 123.°897	271877629. 124.°005	271877681. 124.°324	271878434. 128.°770	
γ Cru	081	i	272320388. 178.°322	272320233. 178.°510	272320226. 178.°519	272320203. 178.°546	272319835. 178.°974	272319448. 179.°397
γ Cru	082	i	272956171. 177.°862	272956016. 178.°056	272956009. 178.°065	272955986. 178.°093	272955617. 178.°532	272955229. 178.°967
RS Cnc	085	i		275057262. 97.°236	275057224. 97.°000	275057119. 96.°337	275055932. 89.°067	275055073. 84.°114
RS Cnc	085	e		275059898. 114.°136	275059935. 114.°371	275060040. 115.°034	275061227. 122.°303	275062086. 127.°256
γ Cru	086	i	275503697. 176.°829	275503542. 177.°033	275503535. 177.°043	275503512. 177.°073		275502756. 177.°995
RS Cnc	087	i					276329999. 92.°710	276328974. 86.°701
RS Cnc	087	e					276334140. 118.°549	276335165. 124.°557
γ Cru	089	i	277408751. 176.°576	277408596. 176.°781	277408589. 176.°791	277408566. 176.°821	277408199. 177.°287	277407813. 177.°749
γ Cru	093	i	280045204. 208.°249	280045028. 208.°061	280045020. 208.°052	280044994. 208.°024	280044576. 207.°598	280044136. 207.°175
γ Cru	094	i	280681410. 191.°683	280681250. 191.°696	280681242. 191.°697	280681218. 191.°699	280680836. 191.°728	280680433. 191.°758
γ Cru	096	i	282014259. 185.°190	282014112. 185.°280	282014104. 185.°285	282014083. 185.°298	282013732. 185.°504	282013362. 185.°708
γ Cru	100	i	285034037. 224.°282	285033857. 223.°835	285033848. 223.°814	285033822. 223.°749	285033398. 222.°741	285032956. 221.°750
γ Cru	101	i	285861190. 224.°289	285861011. 223.°842	285861002. 223.°820	285860976. 223.°755	285860552. 222.°746	285860110. 221.°755
γ Cru	102	i	286686360. 223.°942	286686182. 223.°500	286686173. 223.°479	286686147. 223.°415	286685725. 222.°418	286685285. 221.°438
β Peg	104	i	288914432. 342.°574	288914336. 343.°021	288914332. 343.°042	288914318. 343.°107	288914091. 344.°113	
R Cas	106	i	291039691. 90.°705	291038969. 86.°728	291038939. 86.°566	291038853. 86.°097	291037730. 80.°186	291036830. 75.°723
α Sco	115	i	302022977. 157.°895	302022638. 158.°409	302022621. 158.°434	302022571. 158.°508	302021771. 159.°664	302020939. 160.°797

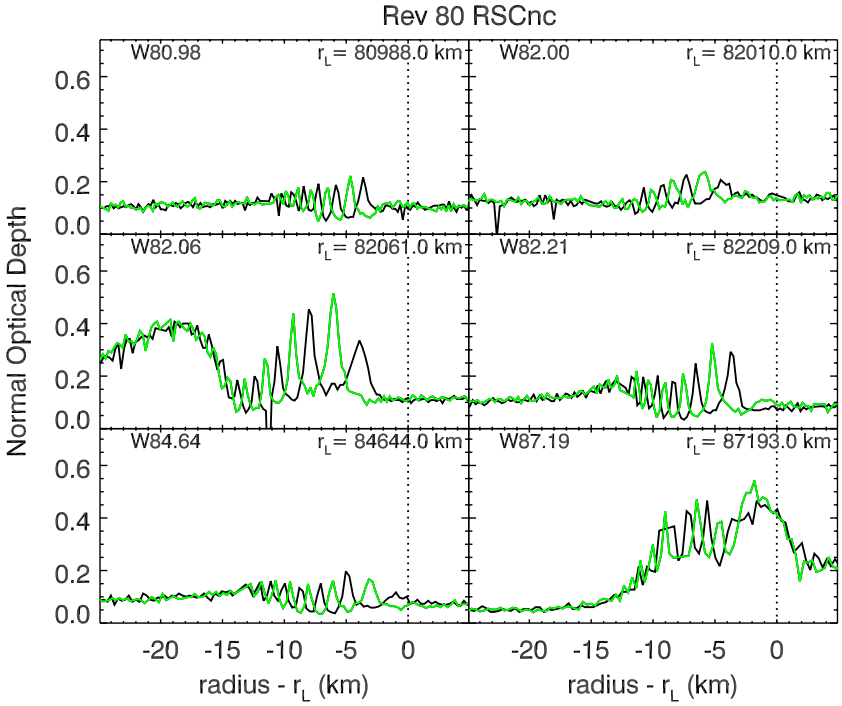

Figure 2. Profiles of the relevant waves obtained during the occultation of the star RS Cancri on Rev 80. The black profiles were obtained during ingress, while the green profiles were obtained on egress. The normal optical depth values assume the star's elevation angle above the rings is 29.°96. Note that the phase differences between the waves seen in ingress and egress are the same for the three waves found around 82,000 km. This suggests that all these waves have the same *m*-numbers.

(A color version and Supplemental data of this figure are available in the online journal.)

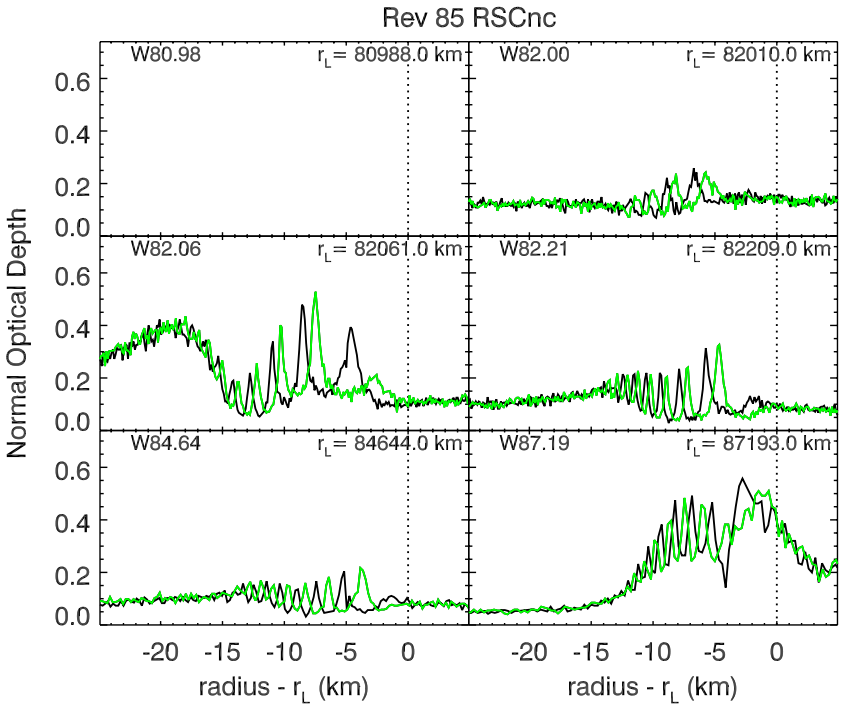

Figure 3. Profiles of the relevant waves obtained during the occultation of the star RS Cancri on Rev 85. The black profiles were obtained during ingress, while the green profiles were obtained on egress. Note that the phase differences between the waves seen in ingress and egress are again the same for the three waves found around 82,000 km. This implies that all these waves have the same *m*-numbers. The two waves found outside 84,000 km also show similar phase differences, indicating that they may have same *m*-number as each other.

(A color version and Supplemental data of this figure are available in the online journal.)

the other and vice versa. This indicates that the phase difference between these two occultation cuts is close to 180° for all three of these waves. This finding alone might be interpreted as a coincidence, but if we turn our attention to the Rev 85 data, we again find suspicious similarities among these three waves. For all three of the waves, the sharp peaks in the egress data occur about one-third of a cycle exterior to the sharp peaks in the ingress data. This again suggests that the phase difference between the ingress and egress cuts (in this case ∼240°) is nearly the same for all three of these waves.

This result is significant because it implies that all three of these waves have the same m-number. The waves W82.00, W82.06, and W82.21 are close together in the rings. Hence, for each of these occultations, the ingress cuts for these three waves occurred at nearly the same longitude and time, and similarly the egress cuts are grouped closely in longitude and time (see Table 2). This means the difference in the observed longitudes ($\delta\lambda$) and the observed times (δt) between ingress and egress are almost identical for the three waves. Since the phase difference between the waves is given by $\delta\phi = |m|(\delta\lambda - \Omega_P \delta t)$, the easiest way for all three waves to have the same phase difference is for them to have the same m-number (which also implies, via Equation (2), nearly identical pattern speeds). Our full analysis of these waves confirms that this is indeed the case.

Being able to determine that W82.00, W82.06 and W82.21 have the same m-number from simple inspection of the RS Cancri profiles is useful because this result does not require the geometry of the occultations to be extremely accurate. The most likely errors in the occultation geometry correspond to shifts in the spacecraft's position along its orbit, which would cause the ingress and egress occultation traces to shift in opposite directions in radius. Such errors will tend to shift the ingress profiles outward or inward relative to the egress curves by the same amount for all three waves. Although the ingress–egress phase differences would then change, as long as the wavelengths are similar this would not change the result that the phase differences between the ingress and egress cuts are nearly the same for all three waves.

3.3. Computing Phase Differences Between Waves

While simple inspection of the RS Cancri profiles suggests that several of the waves have similar pattern speeds and identical m-numbers, we need quantitative measurements of the phase differences between different occultation cuts to ascertain the actual values of m or Ω_p for these waves. Fortunately, we can estimate the phase difference between any two occultation cuts through a given wave using wavelet transforms. A wavelet is basically a localized Fourier transform that can effectively cope with the rapid wavelength changes in typical spiral waves. Indeed, wavelet techniques have already been used to study density waves in order to obtain information about how the radial wavelength varies with distance from the resonance, which can constrain the rings' surface mass density (Tiscareno et al. 2007; Colwell et al. 2009a; Baillié et al. 2011). However, our analysis is different in that it focuses on estimating the *phase difference* between two wave profiles rather than the wavelength or amplitude of the wave.

We perform our wavelet analysis on the raw signal profiles instead of the derived optical depth profiles shown in Figures 1–3. In practice, this choice has little influence on the derived phase differences (the conversion from T to τ just introduces an overall constant phase shift of 180°), but it does eliminate any possible complications that could arise due to the uncertainties in the unocculted star signal. Before applying the wavelet transform to the relevant occultation data, we first interpolate the data onto a uniform array of radii with a radial spacing of 50 m. A small part of this resampled profile centered on each wave (see Table 3 or Table 4 for the exact ranges) is then fed into the publicly available IDL routine `wavelet` (see Torrence & Compo 1998, the default Morlet mother wavelet with $\omega_0 = 6$ is used throughout this analysis). The resulting wavelet is a two-dimensional array of complex numbers as a function of radius and radial wavenumber $\mathcal{W}(r, k)$. (Note that we use the wavenumber k here instead of the wavelength λ in order to avoid any possible confusion with the radiation's wavelength or the longitudinal coordinate.) Let us denote the real and imaginary parts of the wavelet as $\mathcal{W}_R$ and $\mathcal{W}_I$, respectively. We can then define the wavelet power as $\mathcal{P}(r, k) = \mathcal{W}_R^2 + \mathcal{W}_I^2$ and the wavelet phase as $\varphi(r, k) = \tan^{-1}(\mathcal{W}_I, \mathcal{W}_R)$.

Figure 4 illustrates how the wavelet phase and power vary with position and wavelength across the wave. As expected there is a diagonal ridge in the wavelet power that tracks the observed trends in the wave's wavelength. (Recall that for a wave generated at an OLR, the radial wavelength decreases as the wave propagates inward.) Furthermore, we can observe that where the wave is strong and the wavelet power is high, the contours of constant phase are nearly vertical, so a well-defined phase can be ascribed to every radius in the wave. The values of the phase in this region are also reasonable given the profile, being near ±180° at local minima and around 0 at local maxima.[3] Thus, for such waves we can reduce the two-dimensional wavelet to estimates of the wave power and phase as a function of radius by appropriately averaging over a range of spatial wavenumbers.

In order to filter out large-scale background variations in the rings' opacity while still capturing most of the wave's power, we include a limited range of wavenumbers in these averages. Specifically, we exclude all wavenumbers less than $k_1 = 2\pi/(5\text{ km})$ and all wavenumbers greater than $k_2 = 2\pi/(0.1\text{ km})$. The effective power of the wave at a given radius is therefore defined to be

$$P_{\rm eff}(r) = \mathcal{N} \sum_{k=k_1}^{k_2} \mathcal{P}(r, k), \tag{8}$$

where $\mathcal{N}$ is a normalization constant. Note that since we only are interested in relative power for this analysis, we choose $\mathcal{N}$ so that $P_{\rm eff}$ is equal to unity at its peak value. Also note that this sum is done over a series of logarithmically spaced values of k.

In order to derive an effective phase for the wave at each radius, we first compute an effective average real part and imaginary part of the wavelet:

$$W_{R,I}(r) = \frac{\sum \mathcal{W}_{R,I}(r, k)\mathcal{P}(r, k)}{\sum \mathcal{P}(r, k)}, \tag{9}$$

where the sums are again over all values of k between k_1 and k_2. Note these averages are weighted by the power, so that the regions with the strongest signals dominate the averages. From these average wavelet components, we can compute the average phase at each radius:

$$\phi(r) = \tan^{-1}(W_I, W_R). \tag{10}$$

Note that by computing the average of components $\mathcal{W}_I$ and $\mathcal{W}_R$ instead of averaging the local phases $\varphi(r, k)$, we avoid any difficulties involved in averaging a cyclic quantity. The phase difference between two occultations should then simply be the difference in the two values of $\phi(r)$.

Figures 5 and 6 illustrate the results of these calculations for two of the waves seen in the RS Cancri occultation from Rev 85. As expected, there is a peak in the wave power $P_{\rm eff}$ located near the center of the wave. Also, the difference in the wave phase

[3] The wavelet phase also increases with increasing radius, consistent with the expected trend in $\phi(r)$ for a density wave.

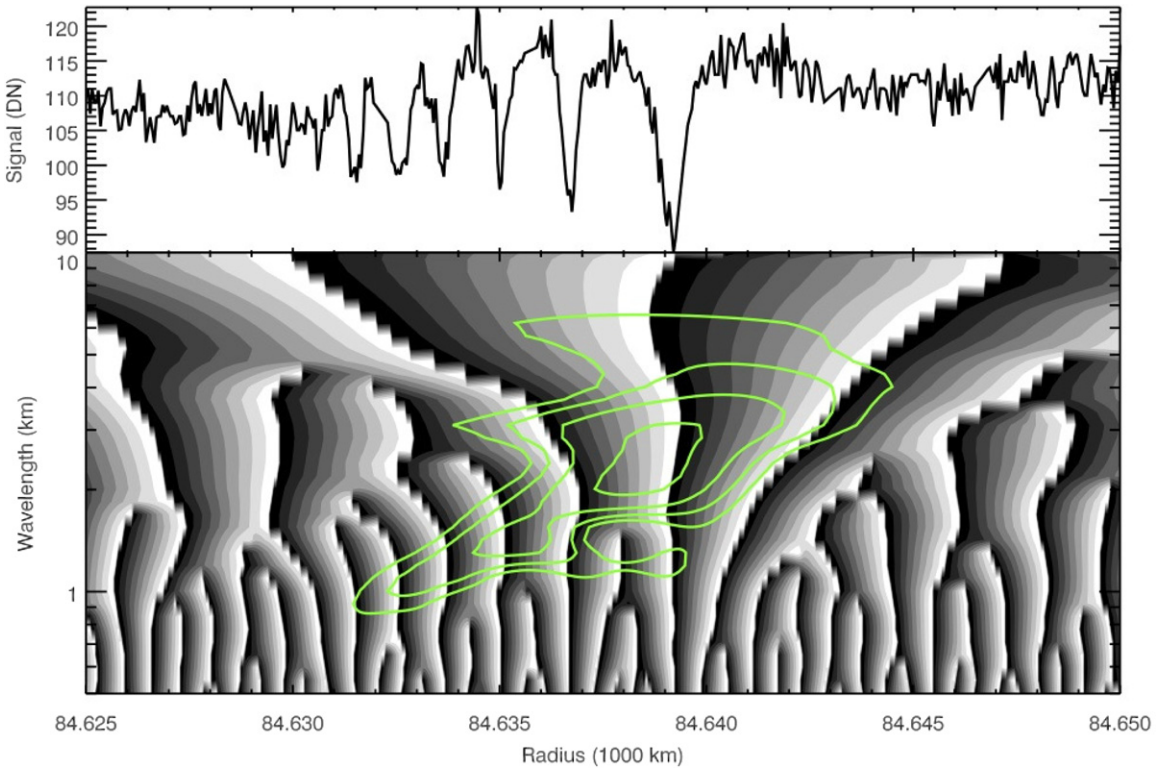

Figure 4. Plot showing the wavelet amplitude and phase derived from the W84.64 wave observed in the Rev 106 RCas occultation. The top panel shows the occultation profile (in raw data numbers, which is proportional to transmission) as a function of radius. The bottom panel shows the wavelet phase and power as functions of radius and spatial wavelength. The wavelet phase is indicated by grayscale levels (black $= -180°$, white $= +180°$) while the overlaid green contours are levels of constant wavelet power. The peak wavelet power follows a diagonal ridge that corresponds to the wave's increasing wavelength with radius. Note that where the wavelet power is strong, the contours of wavelet phase are nearly vertical and correspond to the expected phase of the wave (e.g., the phase wraps from $-180°$ to $180°$ at locations corresponding to sharp minima in the profile).

(A color version of this figure is available in the online journal.)

between the egress and ingress cuts is relatively constant in the region where the wave signal is evident, as desired. Furthermore, the numerical values of these phase differences are consistent with the observed profiles. For the W84.64 wave in Figure 6, the phase difference is around 180°, which is what one would expect given that the peaks in the ingress profile occur at the same location as the dips in the egress profile and vice versa. Similarly, the W82.21 data in Figure 5 yield a phase difference of around 240°, which is consistent with the dips in the egress profile always lying about 1/3 of a cycle exterior to those in the ingress profile. This gives us some confidence that our rather simple approach can extract useful phase information from these wave profiles.

For the purposes of this analysis, we require a single estimate of the average phase difference for any pair of occultation cuts. We estimate this parameter as the weighted average of the phase differences $\delta\phi(r)$, with each of the individual values weighted by the average of the two $P_{\rm eff}$ curves in order to ensure that regions with high signal contribute most to the final estimate. In order to further reduce the possibility of contamination in the phase difference estimate, we only consider regions where the average power of the two waves is more than 0.9 (this threshold is indicated by a dotted line in Figures 5 and 6, and the averaging region is demarcated by vertical dashed lines). Due to the weighting, the resulting estimates of the phase differences are not particularly sensitive to the exact value of this threshold. In addition to computing the weighted average phase difference, $\delta\phi$ between the two cuts (which is shown as a dotted line in the bottom panel of Figures 5 and 6), we also compute the standard deviation of the phase difference values in the selected region σ_ϕ, which quantifies the reliability of the phase estimate. Note, however, that σ_ϕ will underestimate the uncertainty in the $\delta\phi$ because it does not include the effects of uncertainties in the reconstructed geometry. Such geometric uncertainties are difficult to quantify a priori, and will be considered in more detail below.

To recap this procedure, the steps are: (1) compute the wavelet transform, $\mathcal{W}(r, k)$, for each observation and the corresponding power spectrum, $\mathcal{P}(r, k)$. (2) Compute weighted averages for $W_R(r)$ and $W_I(r)$, and thence the average phase $\phi(r)$. (3) Compute the average radial power profile, $P_{\rm eff}(r)$. (4) Compute the average phase difference between two wave profiles $\delta\phi$, weighted by the average of the two power profiles.

3.4. Using Phase Differences to Constrain m-numbers and Pattern Speeds

In order to illustrate how quantitative estimates of $\delta\phi$ can be used to constrain m-numbers and pattern speeds, let us examine the phase differences between the various RS Cancri ingress and egress profiles listed in Table 3. Note that the phase differences for the W82.00, W82.06 and W82.21 waves are indeed very similar for both the Rev 80 cuts (being around $\sim$150°) and the Rev 85 cuts (where they are all $\sim$250°). This is consistent with the above visual inspection of the profiles and supports our contention that these three waves must share a common m-number. However, with these measured values of $\delta\phi$, we can now also identify which values of m and Ω_P come closest to predicting the observed phase differences.

Table 3
Phase Differences Between Ingress and Egress Cuts for the RS Cancri Occultations

Wave	Resonant Location[a]	Region Considered[b]	Rev 80 $\delta\phi$	Rev 85 $\delta\phi$	Rev 87 $\delta\phi$	Possible m-values[c]
W80.98	80988 km	80970–80995 km	141.°6	...	...	−4, −3, +6
W82.00	82010 km	81992–82012 km	148.°5	250.°6	...	−3, +6
W82.06	82061 km	82040–82065 km	148.°1	249.°1	...	−3, +6
W82.21	82209 km	82190–82215 km	150.°1	251.°1	...	−2, −3, +6
W84.64	84644 km	84625–84650 km	145.°4	195.°5	235.°5	−2, +5, +6
W87.19	87189 km	87175–87205 km	... [d]	(182.°2)[e]	191.°4	−2, +5

Notes.
[a] Inferred resonance locations from Baillié et al. (2011, Table 7).
[b] Region over which wavelet power and phase are computed.
[c] m-values between −10 and +10 where the predicted $\delta\phi$ values are within ±30° of the observed values.
[d] Phase difference not determined due to data gap.
[e] Phase difference computed using wavevectors between $k = 2\pi/(0.1\text{ km})$ and $k = 2\pi/(2\text{ km})$ because otherwise combined peak average power is never above threshold.

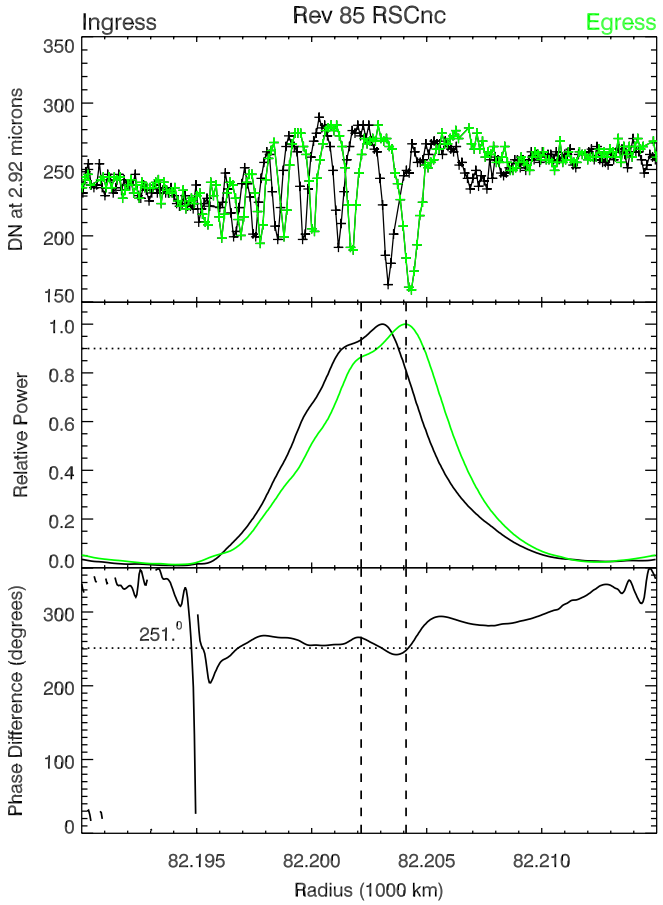

Figure 5. Results of the wavelet calculations of the phase difference in wave W82.21 between the ingress and egress cuts from the Rev 85 RSCnc occultation. The top panel shows the two occultation profiles, while the middle panel shows the integrated wave power $P_{\text{eff}}(r)$ between wavenumbers of $2\pi/(5\text{ km})$ and $2\pi/(0.1\text{ km})$. The bottom panel shows the phase difference $\delta\phi(r) = \phi_{\text{egress}}(r) - \phi_{\text{ingress}}(r)$ between these two cuts (see text for explanations of the dashed and dotted lines). Note that the average phase difference is computed using only the data where the average P_{eff} of the two profiles is above 0.9. The average phase difference is near 240°, which is consistent with the offset between the ingress and egress wave profiles noted in Figure 3.
(A color version of this figure is available in the online journal.)

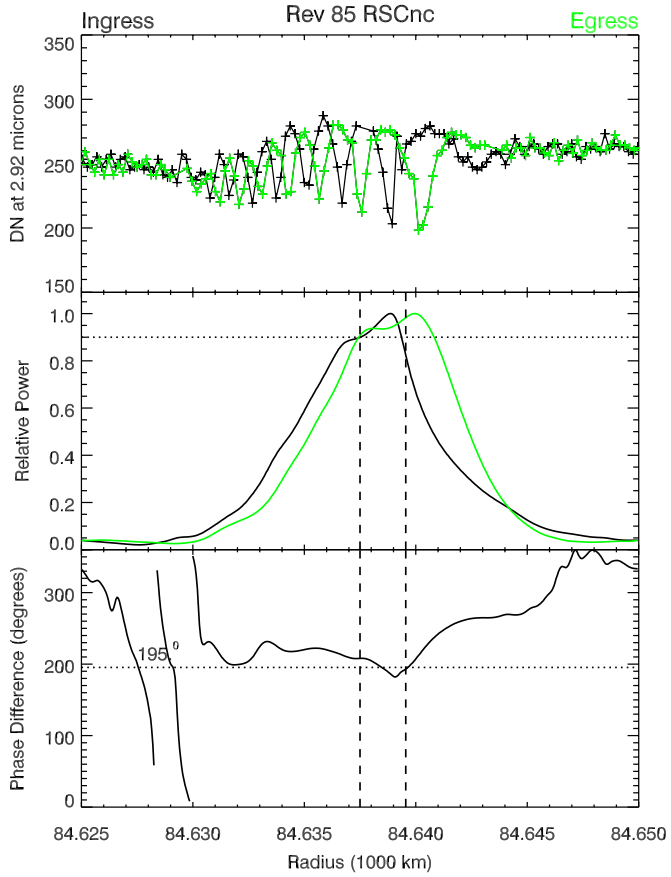

Figure 6. Results of the wavelet calculations of the phase difference in wave W84.64 between the ingress and egress cuts from the Rev 85 RSCancri occultation, following the same layout as in Figure 5. In this case, the average phase difference is near 180°, which is again consistent with the ingress and egress wave profiles.
(A color version of this figure is available in the online journal.)

For any given wave, the local mean motion n and apsidal precession rate $\dot{\varpi}$ of the ring material are straightforward functions of the wave's resonant radius r_L and Saturn's gravitational field (Murray & Dermott 1999). Hence, if we assume the gravitational field parameters given in Jacobson et al. (2006), then we can use Equation (2) to compute the expected pattern speed Ω_P for any given value of m at any of the relevant resonant radii. Furthermore, for a particular pair of occultation cuts, the difference in the observed ring longitudes $\delta\lambda$ and the difference in observation times δt can be obtained from Table 2. We can therefore use the computed pattern speed to calculate the expected phase difference between any two occultation

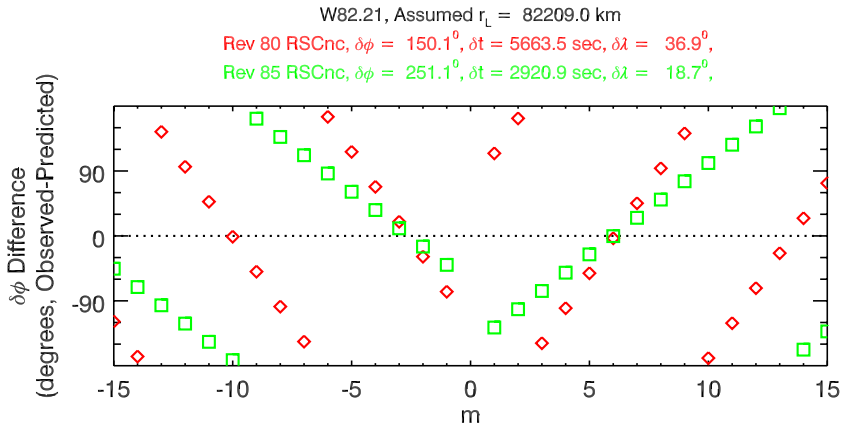

Figure 7. Plot showing the difference between the observed and predicted values of $\delta\phi$ between the ingress and egress cuts of the RS Cancri occultations for the wave W82.21 as a function of the assumed m-number, given the stipulated $\delta\lambda$ and δt values. Different symbols correspond to different pairs of occultation cuts. Note that the residuals for both observations are close to zero when $m = -2$, -3, and +6, so these values of m are the ones most consistent with the observed phase differences.

(A color version of this figure is available in the online journal.)

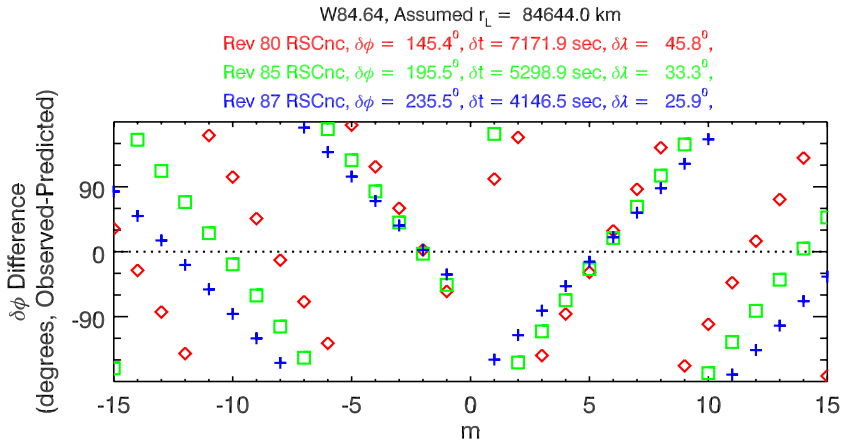

Figure 8. Plot showing the difference between the observed and predicted values of $\delta\phi$ between the ingress and egress cuts of the RS Cancri occultations for the wave W84.64 as a function of the assumed m-number. Note that the residuals for all three observations are close to zero when $m = -2$, +5, and +6, so these values of m are the ones most consistent with the observed phase differences.

(A color version of this figure is available in the online journal.)

cuts $\delta\phi$(predicted) $= |m|(\delta\lambda - \Omega_p \delta t)$ for each value of m (cf. Equation (7)).

Figures 7 and 8 show the differences between the observed and predicted values of $\delta\phi$ for the waves W82.21 and W84.64 as a function of m.[4] For any given observation, the difference $\delta\phi$(observed) $- \delta\phi$ (predicted) cycles repeatedly through 360° with increasing or decreasing m. Hence, there are multiple possible m-values that could be consistent with the single observed phase difference. However, different observations have different values of δt and $\delta\lambda$, and thus show different trends in these plots. Hence, there are relatively few m-values that could be consistent with the two or three observations illustrated in Figures 7 and 8. If we conservatively assume a ±30° uncertainty in the phase determinations (which is consistent with the results of the global analysis described below), then $m = -3$, -2, and +6 are consistent with the RS Cancri observations of the W82.21 wave, and $m = -2$, +5, and +6 are consistent with the observations of the W84.64. The other waves yield similar results, as shown in Table 3. Note that the W82.00, W82.06, and W82.21 waves are consistent with the same set of m-values, as expected

The small number of m-values that are consistent with this limited number of $\delta\phi$ estimates demonstrates that our measurements of $\delta\phi$ can constrain the symmetry properties and pattern speeds of these waves. However, it is also clear that we cannot uniquely determine the m-value for any of these waves with only the RS Cancri data. Thus, the next step in this analysis is to extend this approach to include all pairs of occultation cuts listed in Table 2.

While the procedures described above allow us to calculate $\delta\phi$ for any possible pair of occultation cuts listed in Table 2, in practice some occultation pairs do not yield reliable phase difference estimates. For some pairs, the average wavelet power for the two cuts never exceeds 0.9 of the peak power in each cut. This implies that the peak wave signal in the two cuts is coming from different parts of the wave (perhaps because they have different intrinsic resolutions), and so we do not consider such pairs. We also exclude any occultation pairs which yield an rms phase-difference scatter σ_ϕ greater than 20° because large values of σ_ϕ indicate that the wavelet was unable to identify a consistent phase difference (perhaps due to small gaps or cosmic rays in one of the profiles). Finally, we only consider pairs of occultations

[4] Note that the time elapsed between the ingress and egress cuts can be as much as 2 hr. This is a non-trivial fraction of the 6.5–7 hr orbital period in this region and therefore cannot be ignored in the calculation of the predicted $\delta\phi$.

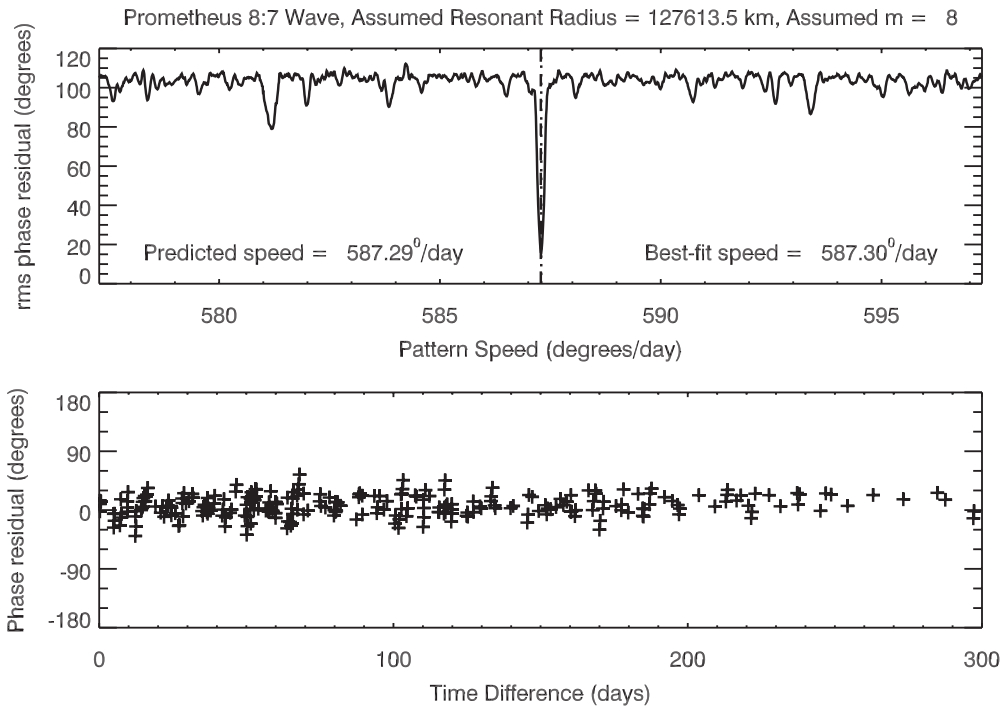

Figure 9. A test of our pattern-speed determination algorithms using the Prometheus 8:7 wave in the inner A ring. The top panel shows the rms phase difference residuals as a function of pattern speed assuming the pattern has an $m = 8$, as expected for this wave. The dashed line marks the predicted pattern speed for this pattern, while the dotted line marks the pattern speed that gives the minimum variance (in this case, these two lines are almost on top of each other). The bottom panel shows the residuals in the phase differences from this best-fit solution as a function of time difference between the pairs of observations. The scatter in these data likely represents residual geometrical uncertainties in the various profiles.

where the time difference is less than 300 days. This prevents any aliasing that might occur due to the limited number of observations with larger time separations. After applying these selection criteria, we have between 100 and 260 $\delta\phi$ estimates for each of the waves (see Tables 4 and 5).

As with the RS Cancri data described above, we constrain the symmetry properties and pattern speeds of each wave by computing expected values of $\delta\phi$ for different combinations of m and Ω_P and comparing these numbers with the observed $\delta\phi$ values. Specifically, we seek values of m and Ω_P that minimize the rms residuals of $\delta\phi$(observed) $-$ $\delta\phi$ (predicted). In principle, we could just compute these rms variations for each m assuming Ω_P is given by Equation (2), as we did for the RS Cancri data. However, given the uncertainties in the planet's gravitational field and the precise locations of the resonant radii for these waves, we will instead compute the rms phase difference residuals over a finite range of pattern speeds surrounding the expected Ω_P corresponding to each m.

Since we are studying patterns that rotate around the planet at hundreds of degrees per day, and we are using occultations separated in time by up to 300 days, it is important to verify that our $\delta\phi$ calculations are sufficiently accurate to yield meaningful constraints on m and Ω_p. This is most easily done by first testing our methods on waves with known pattern speeds. We therefore applied the above algorithms to occultation profiles of the Prometheus 8:7 density wave in the outer A ring. The top panel in Figure 9 shows the rms phase difference residual (observed–predicted) as a function of pattern speed, assuming the pattern has the expected $m = 8$. Note the sharp dip at $587.^{\circ}30\,\mathrm{day}^{-1}$, which corresponds almost exactly to Prometheus' mean motion and the expected pattern speed for this wave. Thus, the pattern speed with the minimum variance in the phase residuals matches the expected perturbation frequency, as desired. Furthermore, no similar dip is seen when other values of m are tried. These results demonstrate that the above procedures can indeed yield reliable estimates for the pattern speeds and m numbers of even tightly wound density waves.

The lower panel of Figure 9 shows the phase difference residuals as a function of time separation δt. These points are randomly scattered about zero, as desired, but with a $\pm 20^{\circ}$ scatter which probably reflects not only statistical uncertainties in the phase estimates themselves but also uncorrected systematic errors in the occultation geometries. As noted above, the latter can shift wave profiles relative to each other, which will produce errors in the phase differences that are hard to model. However, these data demonstrate that these systematic errors do not prevent us from determining the pattern speeds of spiral waves with wavelengths that are sufficiently long. More specifically, the above procedures should yield reliable results so long as the uncertainties in the occultation geometry do not produce phase errors exceeding 90°. As discussed in Section 2.3 above, this should be the case for the six waves considered here.

The small dispersion in the phase difference residuals not only requires accurate phase difference measurements, but the phase differences must also follow the predicted trend given by Equation (7) over a sufficiently long period of time. For waves generated by satellites, the latter condition is equivalent to assuming the relevant moon has a constant mean motion, which is reasonable for most of Saturn's moons (the obvious exceptions being the co-orbitals Janus and Epimetheus, see Tiscareno et al. 2006). For waves generated by planetary normal modes, this condition requires assuming that the relevant oscillation has a constant frequency and a coherent phase over the time period spanned by the observations. This assumption not only turns

out to be consistent with the observations (see below), but it can also be justified a priori based on considerations of the waves' group velocity.

Density waves in dense rings propagate away from the resonance at a finite speed, so any shift in the frequency or phase of the perturbing potential generates discontinuities in the wave's profile (Tiscareno et al. 2006). These features propagate through the rings at the group velocity $v_g \simeq \pi G\sigma_0/\kappa$, where G is the universal gravitational constant, σ_0 the ring's average surface mass density, and κ the radial epicyclic frequency (Shu 1984). For the relevant C-ring waves, σ_0 is between 1 and 10 g cm^{-2} (Zebker et al. 1985; Hedman et al. 2011, Section 5 below), and v_g is between 0.4 and 2.5 km yr^{-1}. The relevant waves extend 10–20 km from the resonances and they do not exhibit any deviations from the expected smooth trends in their wavelengths. Thus, regardless of their origins, the frequencies and phases of the relevant perturbing potentials appear to be coherent over several years. Hence, we are justified in assuming that the phase differences can be predicted using Equation (7) for time intervals of one year or less.

4. RESULTS

We searched for the best-fitting combinations of m numbers and pattern speeds for all six of the waves described in Section 2.3. Given that the wavelength of these waves increases with increasing radius, we expected these patterns would be generated by outer Lindblad resonances, and so the m numbers of these waves would be negative. Also, previous studies of these waves by Rosen et al. (1991) and Baillié et al. (2011) suggested that if $|m|$ was above 5, the implied surface mass density of the C ring would be unreasonably high (see Section 5 below). Finally, the comparison of ingress and egress phases for the RS Cancri occultations in Table 3 suggests plausible values for m of -2, -3 and -4. Thus, we expected that for these waves m would lie between -2 and -5. Nevertheless, for the sake of completeness, we considered all m values between +10 and -10, and searched for minima within 10° day^{-1} of the expected pattern speed given by Equation (2).[5]

For each wave, we found a strong dip in the residual variance for only a single value of m. For wave W80.98, this dip occurred with $m = -4$; for each of waves W82.00, W82.06 and W82.21, it happened with $m = -3$; and for waves W84.64 and W87.19, it was $m = -2$. Figure 10 shows profiles of the rms residuals versus pattern speed for all six waves, assuming the appropriate m-value. The resulting best-fitting pattern speeds can be compared with those calculated for each wave, using the resonance locations specified in Table 7 of Baillié et al. (2011). For all of the waves the minimum in residuals occurs very close to the expected pattern speed. For five of the waves, the best-fit pattern speed is within $0\overset{\circ}{.}08$ day^{-1} of the value predicted using the Baillié et al. (2011) resonance locations, while for the W87.19 wave the best-fit pattern speed is $0\overset{\circ}{.}16$ day^{-1} lower than one would predict using the Baillié et al. (2011) resonance location. These small offsets could represent small errors in either the assumed gravity field or the estimated resonant radii. For example, the offset between the best-fit and predicted pattern speeds for the W87.19 wave could be resolved if the real resonant radius r_L lies just 4 km exterior to the Baillié et al. (2011) estimate of 87,189 km. This wave is superimposed on a peak in optical depth (minimum in transparency), and the resulting variations in the surface mass density across the wave may have complicated earlier efforts to estimate the resonant radius. Indeed, looking at Figures 1–3, the outer edge of this wave could easily fall somewhere around 87,193 km.

Figure 11 shows the individual phase difference residuals as a function of δt for the best-fit solutions. These residuals typically have a spread of approximately $\pm 45^\circ$, which is noticeably larger than that found for the Prometheus 8:7 wave discussed above. This is not entirely surprising given the generally shorter wavelengths and more limited extents of the C-ring waves. Fewer cycles are visible in most occultation profiles of the C-ring waves than for the A-ring wave, so the estimates of the phase differences should be more uncertain. Furthermore, the maximum wavelength of the Prometheus 8:7 wave exceeds 10 km, while the C-ring waves all have maximum wavelengths that are less than 5 km. The estimated phases of the C-ring waves should therefore be more sensitive to small errors in the geometrical reconstructions. Indeed, if we do not include the small corrections to the occultation geometry provided by R. G. French et al. (in preparation), then the rms residuals of the best fit solutions increase by roughly a factor of two. However, even with this increased dispersion, the best-fit solution for each of the six waves remains close to the predicted pattern speed for the appropriate OLR. Hence, our identification of the best-fit m numbers and pattern speeds appears to be robust against any residual uncertainties in the reconstruction geometry.

5. DISCUSSION

Table 4 summarizes the results of this analysis, including the m numbers, pattern speeds Ω_P, and pattern rotation periods ($2\pi/\Omega_P$) for the six waves. We may conservatively estimate the uncertainties in the pattern speeds to be $0\overset{\circ}{.}5$ day^{-1}, since an error in the pattern speed of this magnitude would produce a trend in the residuals that would be clearly detectable in the data (the residuals would reach $\sim 180^\circ$ at 300 days). This is also comparable to the widths of the minima in Figure 10. While the relatively tight distribution of the residuals already gives us some confidence that we have determined the correct values of m and Ω_P for each of these waves, the following considerations lend additional support to these identifications.

1. Each of the pattern speeds is consistent with that calculated for an outer Lindblad resonance at that location for the appropriate m number.
2. Our full analysis indicates that the waves W82.00, W82.06 and W82.21 all have $m = -3$. This is consistent with the similar observed phase shifts between ingress and egress observed for these three waves in the RS Cancri occulations discussed in Sections 3.2 and 3.4. Recall that these arguments were robust against uncertainties in the occultation geometry, and thus provide a useful check on the above analysis.
3. The derived values of m yield plausible values for the C ring's surface mass density.

The last of these three points requires some explanation and qualification. In general, the variation of a wave's wavelength with radius can provide an estimate of the ring's average local surface mass density σ_0 and its mass extinction coefficient τ_n/σ_0, via Equation (6). However, the estimated values of these parameters depend on m, so prior to this work researchers could

[5] We also looked for patterns that would be produced by the higher-order Enceladus 5:1 ($m = 2$, $\Omega_P = 656\overset{\circ}{.}7$ day^{-1}) and the Janus 5:2 ($m = 3$, $\Omega_P = 863\overset{\circ}{.}7$ day^{-1}) inner vertical resonances that lay close to the W80.98 and W82.06 waves. No significant dips in rms residuals were found.

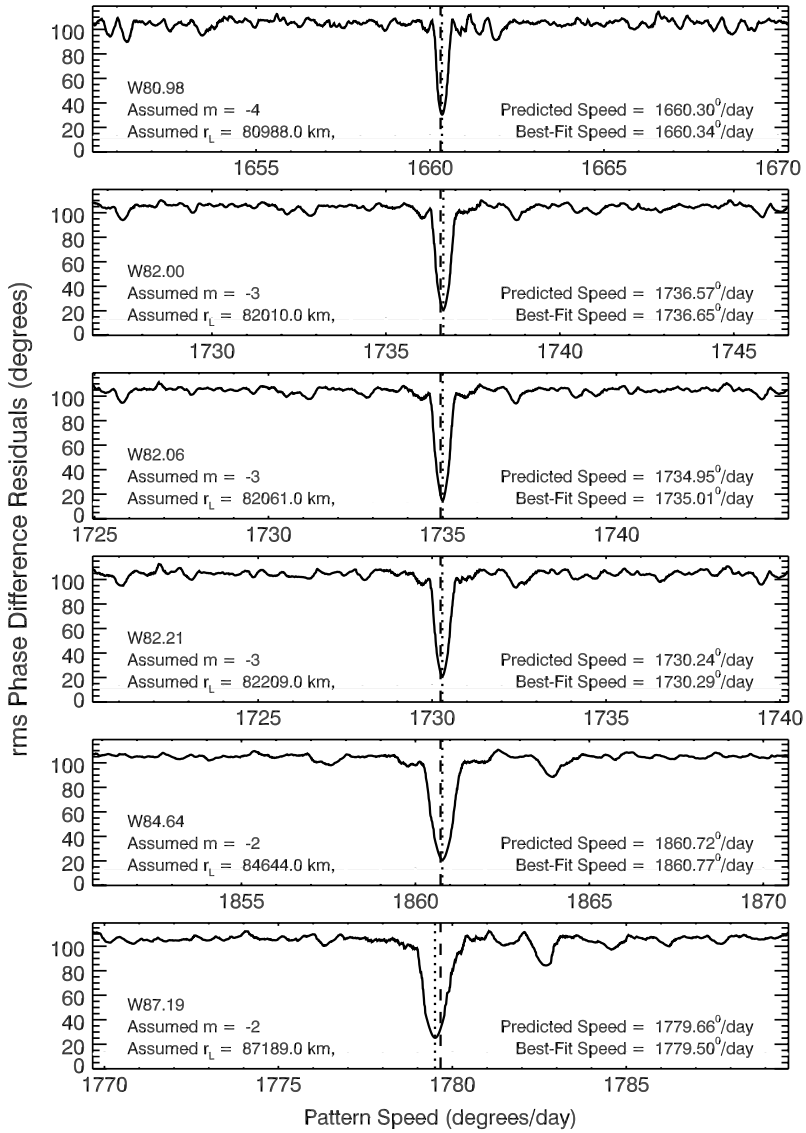

Figure 10. Plots showing the rms phase difference residuals as a function of pattern speed for each of the six waves, assuming the pattern has the indicated m numbers. The dashed line marks the predicted pattern speed for this pattern at the resonant location provided by Baillié et al. (2011), while the dotted line is the pattern speed that gives the minimum variance in the residuals.

only provide estimates of $\sigma_0/|m-1|$ for these six unidentified waves. Table 6 lists the estimates of $\sigma_0/|m-1|$ for all six waves derived by Baillié et al. (2011), and the resulting estimates of σ_0 and τ_n/σ_0 assuming the m numbers derived here.[6] These values can be compared with estimates derived from other features in the rings, but in making these comparisons we must keep in mind that both σ_0 and τ_n/σ_0 may vary with position across the ring.

Studies of the five identifiable C-ring waves by Baillié et al. (2011) yield extinction coefficients ranging between 0.13 and 0.36 cm^2 g^{-1}, which are higher than our estimates. However, most of these identifiable waves occur in very different environments from those occupied by the six unidentified waves considered here. The two waves found near the Mimas 6:2 and Prometheus 4:2 resonances occur within a high-opacity plateau, while the waves associated with the Titan nodal resonance and the Mimas 4:1 resonance are found in rather low optical depth regions interior to 78,000 km. This leaves only the wave associated with the Atlas 2:1 ILR, which is within 500 km of W87.19 and not in a region of obviously elevated optical depth. Intriguingly, Baillié et al. (2011) estimate that $\tau_n/\sigma_0 \simeq 0.19 \pm 0.04$ cm^2 g^{-1} for the Atlas 2:1 wave, which is not too different from the value of 0.11 cm^2 g^{-1} derived above for the nearby W87.19 wave.

For the waves between 79,000 km and 85,000 km there are no known density waves that can provide independent estimates for σ_0 or τ_n/σ_0, but estimates of these parameters have been extracted from other types of observations. Based on the particle size distributions derived from *Voyager* RSS radio occultation data, Zebker et al. (1985) estimated the average surface mass density of the C ring between 78,429 km and 84,462 km to be 3.2 ± 1.8 g cm^{-2}. More recently, Hedman et al. (2011) found that variations in the wavelength of a vertical corrugation extending between 78,000 and 84,000 km indicated that this part of the ring has a mass extinction coefficient of roughly 0.02 cm^2 g^{-1}. Both of these numbers are reasonably consistent with the values of σ_0 and τ_n/σ_0 given in Table 6 for the inner five waves. We thus conclude that the m values derived above do indeed yield plausible values for the mass density of the middle C ring.

[6] Note that, for an OLR, $|m-1|$ becomes $|m|+1$.

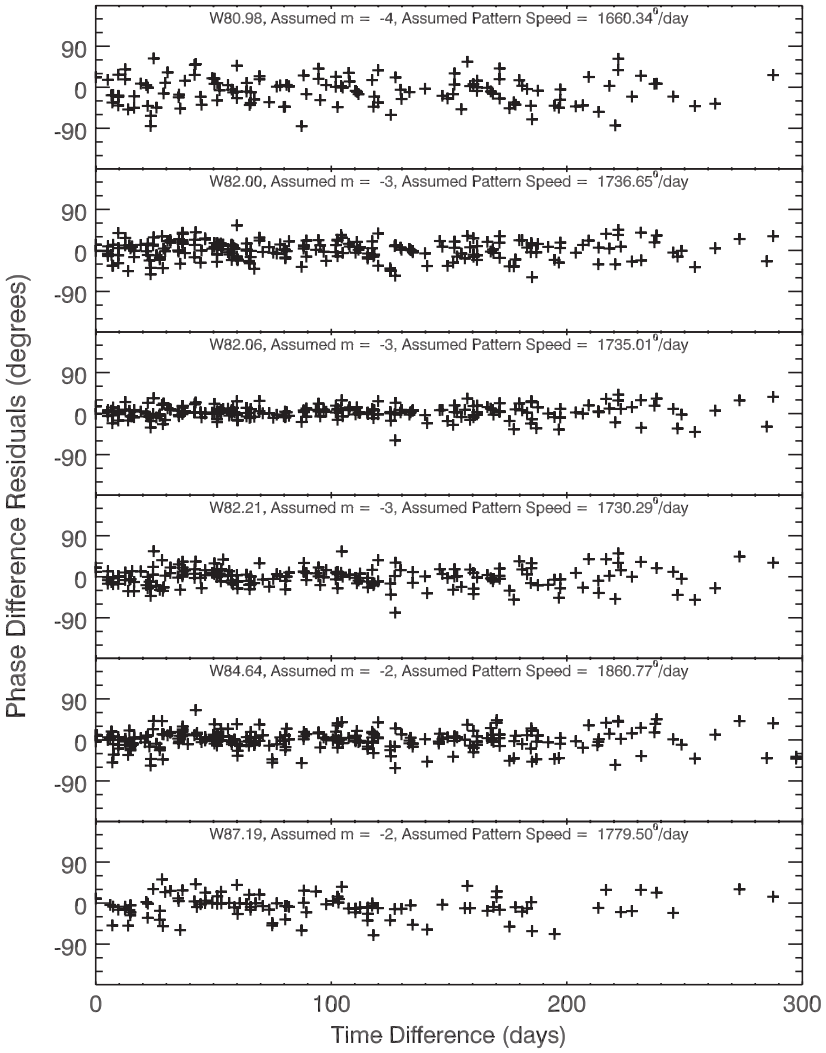

Figure 11. Plots showing phase difference residuals (observed–predicted) for each of the six waves, assuming each pattern has the indicated m number and the pattern speed, which corresponds to the best-fit values shown in Figure 10.

Table 4
Results of the Present Analysis of the Six Waves

Wave	Resonant Location[a]	Region Considered[b]	$N(\delta\phi)$[c]	m	Pattern Speed[d]	Rotation Period
W80.98	80988 km	80970–80995 km	136	−4	1660.3 day^{-1}	312.2 minutes
W82.00	82010 km	81992–82012 km	219	−3	1736.6 day^{-1}	298.5 minutes
W82.06	82061 km	82040–82065 km	217	−3	1735.0 day^{-1}	298.8 minutes
W82.21	82209 km	82190–82215 km	191	−3	1730.3 day^{-1}	299.6 minutes
W84.64	84644 km	84625–84650 km	257	−2	1860.8 day^{-1}	278.6 minutes
W87.19	87189[e] km	87175–87205 km	111	−2	1779.5 day^{-1}	291.3 minutes

Notes.
[a] Resonance locations from Baillié et al. (2011, Table 7).
[b] Region over which the wavelet phase and power are computed.
[c] Number of $\delta\phi$ estimates used in the fits.
[d] Best-fit value. A conservative estimate of the uncertainties in these numbers is 0.5 day^{-1}, which would correspond to a ∼180° residual at 300 days.
[e] The true value may be closer to 87,193 km (see text).

Assuming the above m numbers and pattern speeds are correct, we may now ask what could be producing these waves. They almost certainly cannot be produced by any of Saturn's moons, since such a moon would need to be orbiting just above Saturn's cloud tops, or within the tenuous D ring. Not only have no such moons been detected by *Cassini*, despite extensive imaging of this region, but any kilometer-size icy or rocky objects unfortunate enough to find themselves here would be quickly torn apart by tidal forces.

Instead, these waves may be generated by perturbations from oscillating normal modes within the planet. Indeed, using a particular model for Saturn's internal structure, Marley & Porco

Table 5
Time, Longitude, and Phase Differences Used to Determine Pattern Speeds

Wave	Occultation Pair[a]	δt (days)	$\delta\lambda$ (deg)	$\delta\phi$ (deg)	σ_ϕ (deg)
W82.00	RSCnc085e–RSCnc085i	0.03051	16.9	250.6	3.0
W82.06	RSCnc085e–RSCnc085i	0.03137	17.4	249.1	5.7
W82.21	RSCnc085e–RSCnc085i	0.03381	18.7	251.1	7.7
W84.64	RSCnc087e–RSCnc087i	0.04799	25.9	235.5	4.2
W80.98	RSCnc080e–RSCnc080i	0.05501	31.3	141.6	5.0
W84.64	RSCnc085e–RSCnc085i	0.06133	33.3	195.5	8.9
W82.00	RSCnc080e–RSCnc080i	0.06393	36.0	148.5	8.8
W82.06	RSCnc080e–RSCnc080i	0.06434	36.3	148.1	6.1
W82.21	RSCnc080e–RSCnc080i	0.06555	36.9	150.1	4.3
W87.19	RSCnc087e–RSCnc087i	0.07165	37.9	191.4	12.1
W84.64	RSCnc080e–RSCnc080i	0.08301	45.8	145.4	8.5
W84.64	betGru078i–gamCru078i	0.53957	121.4	47.3	1.7
W84.64	gamCru081i–RSCnc080e	5.10878	50.2	171.7	7.2
W82.21	gamCru081i–RSCnc080e	5.12178	54.2	208.5	4.0
W82.06	gamCru081i–RSCnc080e	5.12265	54.5	136.6	5.9
W82.00	gamCru081i–RSCnc080e	5.12294	54.6	110.6	2.3
W80.98	gamCru081i–RSCnc080e	5.12919	56.8	17.1	11.3

Note. [a] Each occultation is designated by the sequence star-name, REV number and ingress/egress.

(This table is available in its entirety in machine-readable and Virtual Observatory (VO) forms in the online journal. A portion is shown here for guidance regarding its form and content.)

(1993) predicted pattern speeds for a number of normal modes that could produce several of the waves identified in the *Voyager* radio occultation (Rosen et al. 1991). Those authors even suggested that W80.98 might be an $m = -4$ wave generated by a resonance with the $l = 4$ sectoral (i.e., $m = l$) f mode in the planet (which they denote $4f$), and that either W82.06 or W82.20 might be generated by a similar $l = m = 3$ planetary f mode. Indeed, our fitted pattern speeds appear to be very consistent with Marley and Porco's predictions for the pattern speeds generated by normal mode oscillations inside the planet. Their predicted rotation period for the $4f$ mode of 310.6 minutes is quite close to the observed period of 312.2 minutes for the $m = -4$ wave W80.98. Their predicted $3f$ mode period of 296.4 minutes is close to the periods of the $m = -3$ waves W82.00, W82.06, and W82.21, which are 298.5–299.6 minutes. Finally, the predicted $2f$ mode period of 286.4 minutes lies in between the observed periods of our two $m = -2$ waves W84.64 and W87.19. Hence, it seems quite likely that f-mode acoustic oscillations within the planet may be producing these six waves, in which case the precise pattern speeds presented here should be able to help constrain interior models for Saturn. (As but one example, we note that within the range of pattern speeds calculated by Marley (1991) for various Saturn models, those which best fit the observed wave locations correspond to models with no interior differential rotation.)

However, while each of the six waves has a pattern speed that fits with one of the normal modes studied by Marley & Porco (1993), the number of waves associated with each normal mode is much harder to understand. Marley & Porco (1993) predicted that a *single* wave would be associated with each normal mode oscillation. Furthermore, only the f modes with $m = l$ were predicted to have resonances in the C ring (modes with $l > m$ or with internal radial nodes were predicted to have significantly faster pattern speeds and much smaller gravitational signatures). Thus, they expected to find a single wave with $m = -2, -3, -4$, etc. Instead, we find three $m = -3$ waves in close proximity to each other, and two $m = -2$ waves with a larger separation. This suggests that Saturn's internal structure is more complex than Marley and Porco assumed. Thus, future efforts to interpret these findings will likely need to consider the effects of differential rotation, compositional gradients, or a solid core.

At the same time, further investigations of the C-ring waves should provide additional constraints on potential models of Saturn's interior. For example, once more accurate geometric reconstructions of the stellar occultations are available, it should be possible to examine the pattern speeds of shorter-wavelength waves, such as the waves designated "d" and "h" by Rosen et al. (1991) or W85.67 and W83.63 by Colwell et al. (2009b). These particular features could represent additional OLRs with $|m| > 4$ predicted by Marley & Porco (1993). Meanwhile, structures interior to 79,000 km could be generated by vertical resonances with a different class of planetary normal modes. There could even be additional $m = -4, -3$, or -2 patterns lurking within the rings that are either too subtle to detect in individual profiles or obscured by other ring features.

These waves also potentially contain information about the amplitude of the planetary oscillations. All else being equal, a larger-amplitude oscillation in the planet should generate larger fractional density variations in the corresponding density wave. This would imply that the $3f$ oscillations responsible for the W82.21 and W82.06 waves are larger than the one generating the W82.00 wave, and that the $2f$ oscillation responsible for W84.64 is larger than the one that gives rise to W87.19. However, the amplitude of the wave depends not only on the driving torque, but also on how quickly collisions among the ring particles dissipate coherent motions (Shu 1984; Tiscareno et al. 2007). This complicates any effort to extract quantitative estimates of the perturbing force from the wave amplitude, especially for waves that exhibit large fractional density variations, like the ones considered here.

Finally, the ring data can constrain how quickly the oscillations are generated and dissipated within Saturn's interior. As mentioned in Section 3.4 above, the smooth trends in the waves' wavelength with radius indicate that each perturbing potential

Table 6
Ring Mass Density and Extinction Coefficients

Wave	m	$\sigma_0/\lvert m-1\rvert$[a]	τ_n[a]	$(\tau_n/\sigma_0)\lvert m-1\rvert$[a]	σ_0	τ_n/σ
W80.98	−4	1.17 g cm^{-2}	0.13	0.11 cm^2 g^{-1}	5.85 g cm^{-2}	0.022 cm^2 g^{-1}
W82.00	−3	1.42 g cm^{-2}	0.14	0.10 cm^2 g^{-1}	5.68 g cm^{-2}	0.025 cm^2 g^{-1}
W82.06	−3	2.54 g cm^{-2}	0.28	0.11 cm^2 g^{-1}	10.16 g cm^{-2}	0.028 cm^2 g^{-1}
W82.21	−3	1.73 g cm^{-2}	0.13	0.08 cm^2 g^{-1}	6.92 g cm^{-2}	0.020 cm^2 g^{-1}
W84.64	−2	1.35 g cm^{-2}	0.11	0.08 cm^2 g^{-1}	4.05 g cm^{-2}	0.027 cm^2 g^{-1}
W87.19	−2	0.47 g cm^{-2}	0.15	0.33 cm^2 g^{-1}	1.41 g cm^{-2}	0.11 cm^2 g^{-1}

Note. [a] From Table 7 of Baillié et al. (2011).

has maintained a coherent phase for several years. The small dispersion in the phase residuals illustrated in Figure 11 confirms this supposition, and furthermore we find no statistically significant trends in the dispersion with δt out beyond 300 days. If we assume that the planetary oscillations are stochastically excited, then this long coherence time implies a correspondingly high quality factor Q for these oscillation modes. Indeed, given that the oscillation periods of the relevant modes in the planet's frame are ~200 minutes (Marley & Porco 1993), a coherence time in excess of 300 days would imply a $Q > 10{,}000$. This number is comparable to limits computed from the expected tidal evolution of Saturn's moons over the age of the solar system (Dermott et al. 1988) and is comparable to estimates of Jupiter's Q derived from astrometric satellite data (Lainey et al. 2009). However, recent analyses of astrometric measurements of Saturn's moons indicate that Saturn's tidal Q is between 1000 and 2000 (Lainey et al. 2012). These apparently contradictory results might be reconciled if the lower-frequency tidal oscillations are predominantly dissipated by turbulent viscosity acting on inertial waves driven in the convective envelope, as proposed by Ogilvie & Lin (2004). Further analyses of the full span of *Cassini* occultation data should provide novel constraints on dissipation rates within Saturn.

The authors would like to acknowledge discussions with J. Fuller, N. Shabaltas, and D. Lai at Cornell regarding the nature of planetary normal modes and their sensitivity to interior models, which greatly clarified our understanding of these phenomena. We also wish to thank M. Marley for his helpful review of this manuscript. A substantial improvement in our model fits (and reduction of residuals) was achieved using unpublished corrections to the *Cassini* trajectory derived and provided by R. G. French. None of the data analyzed here would have existed without the dedicated work by many individuals on the *Cassini* project as well as the VIMS science and engineering teams. Financial support was provided by NASA.

REFERENCES

Baillié, K., Colwell, J. E., Lissauer, J. J., Esposito, L. W., & Sremčević, M. 2011, Icar, 216, 292
Brown, R. H., Baines, K. H., Bellucci, G., et al. 2004, SSRv, 115, 111
Colwell, J. E., Cooney, J. H., Esposito, L. W., & Sremčević, M. 2009a, Icar, 200, 574
Colwell, J. E., Nicholson, P. D., Tiscareno, M. S., et al. 2009b, in Saturn from Cassini-Huygens, ed. M. K. Dougherty, L. W. Esposito, & S. M. Krimigis (New York: Springer), 375
Dermott, S. F., Malhotra, R., & Murray, C. D. 1988, Icar, 76, 295
French, R. G., Nicholson, P. D., Colwell, J., et al. 2011, in Proc. of EPSC-DPS Joint Meeting (Nantes, France: EPSC-DPS), 2011, 624
Hedman, M. M., Burns, J. A., Evans, M. W., Tiscareno, M. S., & Porco, C. C. 2011, Sci, 332, 708
Jacobson, R. A., Antreasian, P. G., Bordi, J. J., et al. 2006, AJ, 132, 2520
Lainey, V., Arlot, J.-E., Karatekin, Ö., & van Hoolst, T. 2009, Natur, 459, 957
Lainey, V., Karatekin, Ö., Desmars, J., et al. 2012, ApJ, 752, 14
Marley, M. S. 1990, PhD thesis, Arizona Univ., Tucson, AZ
Marley, M. S. 1991, Icar, 94, 420
Marley, M. S., & Porco, C. C. 1993, Icar, 106, 508
Murray, C. D., & Dermott, S. F. 1999, Solar System Dynamics (Cambridge: Cambridge Univ. Press)
Nicholson, P. D., French, R. G., Hedman, M. M., et al. 2011, in Proc. of EPSC-DPS Joint Meeting (Nantes, France: EPSC-DPS), 2011, 632
Ogilvie, G. I., & Lin, D. N. C. 2004, ApJ, 610, 477
Rosen, P. A., & Lissauer, J. J. 1988, Sci, 241, 690
Rosen, P. A., Tyler, G. L., Marouf, E. A., & Lissauer, J. J. 1991, Icar, 93, 25
Shu, F. H. 1984, in Planetary Rings, ed. R. Greenberg & A. Brahic (Tucson, AZ: Univ. Arizona Press), 513
Stevenson, D. 1982, TrAGU, 63, 1020
Tiscareno, M. S., Burns, J. A., Nicholson, P. D., Hedman, M. M., & Porco, C. C. 2007, Icar, 189, 14
Tiscareno, M. S., Nicholson, P. D., Burns, J. A., Hedman, M. M., & Porco, C. C. 2006, ApJL, 651, L65
Torrence, C., & Compo, G. P. 1998, BAMS, 79, 61
Zebker, H. A., Marouf, E. A., & Tyler, G. L. 1985, Icar, 64, 531